Transfer matrices combined with Green's functions for the multiple-scattering simulation of electronic projection imaging

A. Mayer* and J.-P. Vigneron

Laboratoire de Physique du Solide, Facultés Universitaires Notre Dame de la Paix, Rue de Bruxelles 61, B-5000 Namur, Belgium
(Received 23 April 1998; revised manuscript received 2 March 1999)

Electronic projection imaging is described in the framework of a multiple-scattering theory, by using a combination of transfer-matrix and Green's-function formalisms. The transfer-matrix methodology is used to compute the wave propagation within the tip and object scattering region, while the Green's-function formalism is used to describe the electron projection from the scatterers towards a distant imaging screen. This full-order theory is needed to overcome the limits of the first Born approximation and deal with three-dimensional effects. In particular, this approach is able to account for sucking-in and standing-wave effects taking place close to or inside the object. The simulation of the electronic diffraction by a model nanoscopic carbon rod, eventually containing inhomogeneities, is considered in detail. [S0163-1829(99)11527-3]

I. INTRODUCTION

Projection microscopes make use of the quasiradial far propagation of field-emitted [1–9] electrons or ions projected out of small tips. Greatly magnified shadows[10] of an object can be obtained, without any lens, on a distant screen by placing the object at short distances from the tip, inside the electron beam. By using technologies developed for the scanning tunneling microscope, tip-sample distances can be controlled within one angstrom precision, resulting in magnifications of the order of $10^5 - 10^6$ for carbon fibers with diameters between 10 and 20 nm.

In the Fresnel projection microscope (FPM),[11] the electronic source is a tungsten 2 to 3 nm height pyramidal nanoprotrusion with single atom sharpness, hereafter called nanotip.[12–16] The object lays on a 3 mm TEM gold grid and the screen is a 10 cm distant multiple-channel-plate coupled to a fluorescent screen. The field emission voltage, established between the tip holder and the object supporting grid, is adjusted in the range of 50–300 V, a bias which is low enough to avoid all risks of sample destruction. The atomic size of the emission area is responsible for the high coherence,[17] the stability, and the tiny energy dispersion (100 meV at room temperature) of the electronic beam. For small tip-sample distances, the incoming wave is essentially spherical, giving rise to Fresnel diffraction images, still highly correlated with direct-space representation images of the object.

The diffraction fringes observed in experimental figures[11] indicate the relevance of the wave behavior of electrons for the understanding of the image formation. Reasonable agreement with experimental results was achieved within the Fresnel-Kirchhoff flat-object formalism,[18] which assumes a point source and reduces the object to a two-dimensional mask defining an empirical transmission function. While this method gives good results for homogeneous materials, it does not take account of the three-dimensional distribution of the object scattering strength and is then not suited for the description of heterogeneous materials. Furthermore, this formalism is not aware of the strongly varying electric field

distribution around the tip and the sample, mainly responsible for the position of the virtual projection point[11] and the focusing effect observed with small transparent carbon fibers.[19]

In this paper, we propose a method that takes us beyond the Fresnel-Kirchhoff formalism, by bringing into the theory the detailed three-dimensional electron potential-energy distribution between the metallic tip holder and the object support conducting grid. Furthermore, we remove the assumed empirical point source by enforcing that the spatial current density results from realistic traveling electrons provided by the metal tip holder and emitted into the accelerating electric field defined by the tip and the sample. The sucking-in effect and all effects due to the three-dimensional distribution of the scattering power in the sample are the main subjects of discussion brought to light by this model.

In order to reach these objectives, we had to develop a formalism, which happens to be a combination of state-of-the-art transfer-matrix and Green's-function scattering formalisms (see Sec. II). The Green's-function formalism[20–26] is well suited to propagate the wave function from the main scattering region (i.e., the region between the metallic tip holder and the conducting grid) to the imaging screen. Within the scatterer, however, the Green's-function formalism should not be recommended: since the relevant potential energy cannot be kept localized in space, the Green's-function scattering computation would therefore require prohibitively large data storing. In a transfer-matrix method,[27–33] the three-dimensional problem is reduced to a discrete set of coupled one-dimensional problems, using a basis-set expansion to describe the electron lateral behavior and a direct-space analysis in the forward direction. If properly implemented,[30] this approach appears to be very well suited to the description of wave propagation in complex scattering domains, as it requires only two-dimensional amounts of storage space, compared to Green's-function three-dimensional requirements. The transfer-matrix formalism is, by contrast, not effective to propagate the wave function over very large distances. In our description of the projection imaging process, we then choose to use both methods, devoting them to handle that part of the computa-
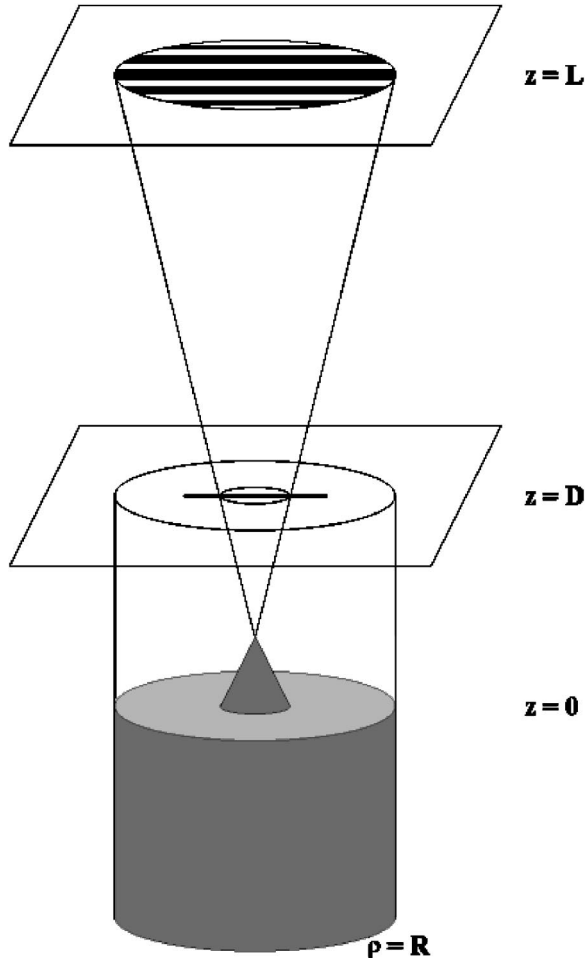
FIG. 1. Virtual projection microscope. Electrons are emitted from a small tip, which stands on the flat surface ($z=0$) of a Sommerfeld metal. After a multiple scattering process below the sample supporting grid ($z=D$), the electrons propagate freely to an imaging screen ($z=L$), where a projected image of the sample is obtained. In the region below the sample support ($z \leq D$), the electrons are confined in a cylinder with radius R.

tion for which each of them is the most efficient.

In Sec. III, we explore the image formation when the object is a long homogeneous or inhomogeneous rod with a square section a few electron wavelengths wide. We will first closely examine a few effects specifically due to three-dimensional multiple scattering, including the observed electron wave focusing by the object, usually described as a ''sucking in'' effect. Thereafter, we focus on the resolution power of the electronic projection microscope and investigate the question of reaching atomic resolution. For the geometry at hand, it is shown that atomic scale details are not obviously apparent in the multiple-scattering images, a limitation which remains consistent with the predictions of a more simple Fresnel-Kirchhoff theory.

II. THEORY

A. Preliminaries

The virtual instrument considered in the present paper is depicted in Fig. 1. Electrons are provided by a ''Sommerfeld'' metal at $z<0$ (region I), emitted through a very narrow

tip and scattered by a three-dimensional object in region II, which ends at $z=D$ (typically $D=10$ nm, including the 2 nm tip), and finally projected through a zero potential region III to be received by a screen at $z=L$ (typically $L=10$ cm). A typical bias of a few tens or hundreds of volts is applied between the metallic tip holder and the object support plane.

Supporting the field-emission tip, the metal is described as a region (region I) of constant potential energy V_{met}, using a simple Sommerfeld model characterized by measured values of W (work function) and E_F (Fermi energy). The conducting grid is described by the plane $z=D$. In the region $z>D$ (region III), where the potential energy is set conventionally to the constant value 0, the electrons escaping from the object travel freely without any further scattering.

In the intermediate region $0 \leq z \leq D$ (region II), which contains the emission nanotip and the sample, the potential energy is written $V(\mathbf{r})$. This potential, of electrostatic origin, can be computed by applying overrelaxation methods[34,36] (when the object or the tip is described as a continuous medium) or by dipole self-adjustment methods[35] (for a discrete atomistic view of the object or tip structures).

B. Wave-function expansion

The discrete atomic structure of the emitting device often leads to situations where the relevant part of the system can be described as invariant under finite rotations. In order to take advantage of such situations, the one-electron scattering problem is formulated in cylindrical coordinates, by using the z axis as the axial direction. The polar coordinates in the plane normal to this n-fold symmetry axis are denoted ϕ (azimuthal angle) and ρ (radial distance to the axis).

The wave function is then expanded in terms of basis functions that account for the ϕ and ρ dependences. Since a continuum of such basis functions would not be easy to handle numerically, their set is forced to be enumerable, by specifying that the scattering electron remains localized inside a cylinder with radius R (Ref. 34) in the regions I and II. The wave function in these two regions then takes the form

$$\Psi(\mathbf{r}) = \sum_m \sum_j \Phi_{m,j}(z) \Psi_{m,j}(\rho, \phi). \tag{1}$$

In this last expression, the two integer subscripts m and j enumerate the basis functions $\Psi_{m,j}(\rho, \phi)$, given by

$$\Psi_{m,j}(\rho, \phi) = \left(\frac{J_m(k_{m,j}\rho)e^{im\phi}}{\sqrt{2\pi \int_0^R \rho[J_m(k_{m,j}\rho)]^2 \, d\rho}} \right) \tag{2}$$

characterized by a radial wave vector $k_{m,j}$ solution of $J_m'(k_{m,j}R)=0$. The z dependence of the wave function is contained in the coefficients $\Phi_{m,j}(z)$ of the expansion. The products $\Phi_{m,j}(z)\Psi_{m,j}(\rho, \phi)$ will be referred to as ''states'' of the wave function.

Requiring, as boundary condition, the basis functions to have a vanishing radial derivative at $\rho=R$, has some advantage over cancelling the function itself. This condition turns out to be less stringent, since only the current density along ρ is forced to vanish, while cancelling the function would force all components of the current density to vanish. The root

$k_{0,0}=0$, corresponding to a wave-function component with a purely axial wave vector, characterizes the main part of the wave function and is skipped by the representation when the cancellation of the basis functions instead of their derivatives is set as a boundary condition.

C. Propagation equations

Let us expand the n-fold symmetric potential-energy distribution $V(\rho,\phi,z)$ in the form

$$V(\rho,\phi,z)=V_0(z)+\sum_{q=-\infty}^{+\infty}\bar{V}_q(\rho,z)e^{iqn\phi}, \qquad (3)$$

where the choice of $V_0(z)$ is arbitrary, but should correspond to the main part of the potential energy since this part enters the propagation equations analytically.

Using expression (1) for the wave function and expression (3) for the potential energy in the stationary Schrödinger equation, the wave-function expansion coefficients $\Phi_{m,j}(z)$ turn out to verify the exact set of coupled equations:

$$\frac{d^2\Phi_{m,j}(z)}{dz^2}+\left[\frac{2m}{\hbar^2}E-k_{m,j}^2-\frac{2m}{\hbar^2}V_0(z)\right]\Phi_{m,j}(z)$$

$$=\sum_q\sum_{j'}M_{m,j}^{q,j'}(z)\Phi_{m-qn,j'}(z), \qquad (4)$$

where E is the electron energy and the coupling coefficients $M_{m,j}^{q,j'}(z)$ are defined by the expression

$$M_{m,j}^{q,j'}(z)=\frac{2m}{\hbar^2}\frac{\int_0^R\rho\bar{V}_q(\rho,z)J_m(k_{m,j}\rho)J_{m-qn}(k_{m-qn,j'}\rho)d\rho}{\sqrt{\int_0^R\rho[J_m(k_{m,j}\rho)]^2\,d\rho}\sqrt{\int_0^R\rho[J_{m-qn}(k_{m-qn,j'}\rho)]^2\,d\rho}}. \qquad (5)$$

The advantage of the n-fold symmetry assumption lays in the fact that coupling between different components of the wave function occurs only when the corresponding m subscripts are separated by a multiple of the symmetry axis order n. There are therefore n independent groups of coupled components, which can be treated separately. Details on the derivation and use of Eqs. (4) and (5) are given in Refs. 35 and 36.

D. Local scattering by the transfer-matrix methodology

The current density obtained on the screen is due to the contribution of all incident states in the metal. These states are scattered in region II and propagate freely in region III to the screen. The underlying Schrödinger equation being linear, the scattering in region II can be treated in the framework of transfer matrices. The propagation to the screen will be achieved in the next section, by using the Green's-function formalism. At this stage, we just need an expression of the wave-function corresponding to each incident state at $z=D$.

Since the potential energy remains constant in region I, the wave function expansion coefficients take the form

$$\Phi_{m,j}^{I}(z)=A_{m,j}^{I}e^{i\sqrt{2m/\hbar^2(E-V_{met})-k_{m,j}^2}\,z}$$

$$+B_{m,j}^{I}e^{-i\sqrt{2m/\hbar^2(E-V_{met})-k_{m,j}^2}\,z}. \qquad (6)$$

Let us take at $z=D$ the following expression:

$$\Phi_{m,j}^{III}(z)=A_{m,j}^{III}e^{i\sqrt{(2m/\hbar^2)E-k_{m,j}^2}\,z}$$

$$+B_{m,j}^{III}e^{-i\sqrt{(2m/\hbar^2)E-k_{m,j}^2}\,z}. \qquad (7)$$

In these expressions, the roots $\sqrt{2m/\hbar^2(E-V_{met})-k_{m,j}^2}$ and $\sqrt{2m/\hbar^2E-k_{m,j}^2}$ are positive reals or complex numbers with positive imaginary parts.

Due to the linearity of the propagation equations, region II can be described by four transfer matrices that contain the expansion coefficients in Eqs. (6) and (7) corresponding to the transmitted and reflected parts of the wave function when a single incident state with unit amplitude encounters region II.

When the incident state (corresponding to a single basis function with subscripts $\bar{m}$ and $\bar{j}$) is coming from $z=-\infty$, the wave function is written as

$$\Psi_{\bar{m},\bar{j}}^{+}(\mathbf{r})\overset{z\leqslant0}{=}\sum_{m,j}\left(\delta_{(m,j),(\bar{m},\bar{j})}e^{i\sqrt{2m/\hbar^2(E-V_{met})-k_{m,j}^2}\,z}\right.$$

$$\left.+t_{(m,j),(\bar{m},\bar{j})}^{-+}e^{-i\sqrt{2m/\hbar^2(E-V_{met})-k_{m,j}^2}\,z}\right)\Psi_{m,j}(\rho,\phi)$$

$$\overset{z=D}{=}\sum_{m,j}\left(t_{(m,j),(\bar{m},\bar{j})}^{++}e^{i\sqrt{2m/\hbar^2E-k_{m,j}^2}\,z}\right)\Psi_{m,j}(\rho,\phi). \qquad (8)$$

No wave-function component coming backwards from $z=+\infty$ is to be considered.

To compute the two transfer matrices $\mathbf{t}^{++}$ and $\mathbf{t}^{-+}$, the peculiar solutions corresponding to a single outgoing state with unit amplitude at $z=D$ has to be constructed. Since the wave function at this interface is entirely defined, the wave-function expansion coefficients $\Phi_{m,j}(z)$ and their derivatives are known at $z=D$. By using these boundary values and Eqs. (4) and (5), the wave-function expansion coefficients $\Phi_{m,j}(z)$ can be propagated by appropriate numerical techniques[35,36] to $z=0$ and written in the same form as ex-

pression (6). By considering separately all possible outgoing states at $z=D$, one obtains the following set of solutions:

$$
\bar{\Psi}_{m,\bar{j}}^{+}(\mathbf{r}) \overset{z \leq 0}{=} \sum_{m,j} (A_{(m,j),(\bar{m},\bar{j})} e^{i\sqrt{2m/\hbar^2(E-V_{\mathrm{met}})-k_{m,j}^2}z}
$$

$$
+ B_{(m,j),(\bar{m},\bar{j})} e^{-i\sqrt{2m/\hbar^2(E-V_{\mathrm{met}})-k_{m,j}^2}z}) \Psi_{m,j}(\rho,\phi)
$$

$$
\overset{z=D}{=} \sum_{m,j} (\delta_{(m,j),(\bar{m},\bar{j})} e^{i\sqrt{(2m/\hbar^2)E-k_{m,j}^2}z}) \Psi_{m,j}(\rho,\phi).
$$

(9)

Taking into account the linearity of the propagation equations, it is possible to combine the solutions given in Eq. (9) to obtain solutions in the form (8). The relevant relations are

$$
\mathbf{t}^{++} = \mathbf{A}^{-1},
$$

$$
\mathbf{t}^{-+} = \mathbf{B}\mathbf{A}^{-1}.
$$

(10)

The two transfer matrices $\mathbf{t}^{--}$ and $\mathbf{t}^{+-}$ that contain the coefficients of the transmitted and reflected parts of the wave functions corresponding to a single incident state with unit amplitude coming from $z=+\infty$ are obtained in a similar way. An efficient technique to control the numerical instabilities encountered in the computation of the transfer matrices is presented in Ref. 27.

E. Propagation to the screen by the Green's-function methodology

The requirement that the basis-function set is enumerable leads to the assumption that the electrons are confined inside a cylinder with finite radius R. This assumption is adequate as long as the wave function naturally disappears for radial distances ρ smaller than R. For a field-emission situation, this last condition is fulfilled until the electronic beam reaches the cylinder boundary. At this stage, a reflection of the beam occurs and makes the resulting wave function meaningless. This is the reason why a solution cannot be obtained on the 10 cm distant screen with the previous transfer-matrix formalism.

Within the Green's-function formalism, it is possible to derive the expression of a wave function at an arbitrary position of space $\mathbf{r}$ by using its expression on a closed surface S surrounding the position considered. The relevant expression, derived in Appendix A, is the following:

$$
\int\int_{S} \mathbf{n}\cdot[G(\mathbf{r}',\mathbf{r},E)\nabla_{\mathbf{r}'}\Psi(\mathbf{r}')
$$

$$
-\Psi(\mathbf{r}')\nabla_{\mathbf{r}'}G(\mathbf{r}',\mathbf{r},E)]dS' = -\frac{2m}{\hbar^2}\Psi(\mathbf{r}),
$$

(11)

where $\mathbf{n}$ is a unit vector normal to the surface and oriented outwards.

Let us consider a point $\mathbf{r}$ on the screen in region III and take for S a surface that contains the plane $z=D$ and is closed at $\rho=\infty$ on the surface $z=+\infty$. The wave function on

this surface takes nonzero values only in the circular aperture defined by the intersection between the plane $z=D$ and the cylinder with radius R, so that the previous expression becomes

$$
\Psi(\mathbf{r}) = \frac{\hbar^2}{2m}\int\int_{\mathrm{circ\,apert}}
$$

$$
\times\left(G(\mathbf{r}',\mathbf{r},E)\frac{d\Psi(\mathbf{r}')}{dz'} - \Psi(\mathbf{r}')\frac{dG(\mathbf{r}',\mathbf{r},E)}{dz'}\right)dS'.
$$

(12)

Since the potential energy in the region III takes the constant value $V=0$ and the wave function and its derivatives cancel at infinite distances in this region, the Green's function G to consider is given by

$$
G(\mathbf{r}',\mathbf{r},E) = -\frac{m}{2\pi\hbar^2}\frac{1}{|\mathbf{r}'-\mathbf{r}|}e^{i\sqrt{(2mE/\hbar^2)}|\mathbf{r}'-\mathbf{r}|}.
$$

(13)

Due to the large metal-screen distance (compared with the cylinder radius R), the factor $|\mathbf{r}'-\mathbf{r}|$ can be expanded as

$$
|\mathbf{r}'-\mathbf{r}| = |\mathbf{r}| - \mathbf{r}^0\cdot\mathbf{r}' + \frac{1}{2|\mathbf{r}|}[|\mathbf{r}'|^2-(\mathbf{r}^0\cdot\mathbf{r}')^2]+\cdots, \quad (14)
$$

where $\mathbf{r}^0$ is a unit vector with components $(1,\theta,\phi)$ in spherical coordinates that points to $\mathbf{r}$ from the origin. The third term in this expression is of the same order as the second for a critical distance from the grid around $d_{\mathrm{crit}}\sim|\mathbf{r}'|/2\sim R/2$. The solution becomes radiative when it becomes less than 1% of the second term, i.e., for a distance $d_{\mathrm{rad}}=50R$. For a screen distance of 10 cm, the third term is less than 10^{-7} of the second (for a maximal value of $R=20$ nm), so it is negligible.

With this approximation in expression (13), Eq. (12) becomes

$$
\Psi(r,\theta,\phi) = -\frac{1}{4\pi r}e^{i\sqrt{2mE/\hbar^2}[r-\cos(\theta)D]}
$$

$$
\times\int_0^R\int_0^{2\pi}\left(\frac{d\Psi(\rho,\phi',D)}{dz'}\right.
$$

$$
\left.+i\Psi(\rho,\phi',D)\sqrt{\frac{2mE}{\hbar^2}}\cos(\theta)\right)
$$

$$
\times e^{-i\sqrt{2mE/\hbar^2}[\rho\cos(\phi'-\phi)\sin(\theta)]}\rho\,d\rho\,d\phi'.
$$

(15)

Within the Kirchhoff approximation,[37] we can now use the wave-function expansion (8) (i.e., the values of the wave function and its derivatives) in this last result to derive its expression on the screen:

$$
\Psi_{m,\bar{j}}^{+}(r,\theta,\phi) \overset{r \gg 0}{=} \frac{e^{ik_E r}}{r}\sum_{m,j} t_{(m,j),(\bar{m},\bar{j})}^{++}\sigma(\theta,m,j,E)e^{im\phi}
$$

(16)

with $k_E = \sqrt{2mE/\hbar^2}$, and

$$\sigma(\theta,m,j,E) = -\frac{e^{-ik_E\cos(\theta)D}}{2}[\sqrt{k_E^2-k_{m,j}^2}+k_E\cos(\theta)]$$

$$\times i^{1-m}\frac{e^{i\sqrt{k_E^2-k_{m,j}^2}D}}{\sqrt{2\pi\int_0^{2\pi}[J_m(k_{m,j}\rho)]^2\rho\,d\rho}}$$

$$\times\int_0^R d\rho\,\rho J_m(k_{m,j}\rho)J_m(k_E\sin(\theta)\rho). \tag{17}$$

F. Computation of the total current density

Each incoming state in the metallic support gives rise to transmitted states. The only incoming states to consider are those associated with a real value of $\sqrt{2m/\hbar^2(E-V_{\mathrm{met}})-k_{m,j}^2}$. Considering the expression (16) and the transfer matrix $\mathbf{t}^{++}$, it is easy to compute the corresponding current density $\mathbf{J}_{m,j}^+(\mathbf{r})$.

Taking into account the absence of correlation between the incoming states in the metal and their contribution to the density of states, the current density corresponding to all incident states with energy E is obtained by the weighted sum[35,36]

$$\mathbf{J}_E(\mathbf{r}) = \frac{m}{(R\hbar\pi)^2}\sum_m\sum_j\frac{1}{\sqrt{\frac{2m(E-V_{\mathrm{met}})}{\hbar^2}-k_{m,j}^2}}\mathbf{J}_{m,j}^+(\mathbf{r}). \tag{18}$$

In this one-electron model, the basis functions are constructed so that the particle probability density of the associated state, when integrated on a given cylindrical section of the metal, gives all the same result. Each state can be considered to be representative of the same number $|A|^2$ of electrons in a unit volume of the metal. For the description to be appropriate, we can multiply each basis function by the common factor A, determined by the requirement that the particle probability density, when integrated over all possible states and energies in the metal, provides the correct value:

$$\rho_{\mathrm{met}} = \frac{1}{3\pi^2}\left(\frac{2mE_F}{\hbar^2}\right)^{3/2}. \tag{19}$$

The factor A is given by the relation[35,36]

$$\rho_{\mathrm{met}} = |A|^2\frac{2m}{(R\hbar\pi)^2}\int_0^{E_F}dE\sum_j\frac{1}{\sqrt{\frac{2mE}{\hbar^2}-k_{0,j}^2}}$$

$$\times\left(2\pi\int_0^R\rho[J_0(k_{0,j}\rho)]^2\,d\rho\right)^{-1}. \tag{20}$$

These coefficients can be computed analytically by using Lommel integrals.[38]

Finally, the total electric current density is obtained by integrating over the energy continuum in the metal:

$$\mathbf{j}(\mathbf{r}) = e\int_{V_{\mathrm{met}}}^{V_{\mathrm{met}}+E_F}\mathbf{J}_E(\mathbf{r})\,dE. \tag{21}$$

III. APPLICATION: OBSERVATION OF A CARBON FIBER BY PROJECTION MICROSCOPY

Under appropriate conditions, electronic projection microscopes provide Fresnel diffraction figures strongly correlated with the object diffusion strength distribution under investigation. This essential feature can be traced to the spherical shape and coherence of the electronic waves, when incident on the object. The necessity to use nanotips with a monatomic termination in order to obtain well contrasted diffraction fringes was already demonstrated.[39] The present application focuses on the relation between the characteristics of the diffraction figures and the properties of the sample, when the conditions enable Fresnel diffraction.

One property that turns out to be important in the image formation is the polarization of the matter. The effects of this polarization are more pronounced for small samples (i.e., carbon fibers with a thickness of a few nm) and result in a ''sucking-in'' effect, which is due to the attraction of the traveling electrons by the electric field surrounding the sample.

The images obtained with carbon fibers depict a homogeneous material and do not provide direct information on the underlying atomic structure. The reason comes from the limited resolution of the technique, which usually does not enable the observation of structures smaller than 0.5 nm. An expression for the resolution limit due to diffraction in a projection configuration was derived within the Fresnel-Kirchhoff flat-object formalism.[18] If λ is the electronic wavelength in the sample and d the distance between this sample and the point source, the resolution of the projected image is $\Delta_d = \frac{1}{2}\sqrt{\lambda d}$. For Fresnel diffraction to occur, this value has to be less than one-half of the sample thickness. When this condition is fulfilled, each point in the projected image turns out to be associated approximatively with a spherical region in the sample, whose radius is Δ_d. Each point in the image gives, therefore, an averaged piece of information on the sample (i.e., a result that depends on the contents of the associated sphere in the sample), excluding the possibility to detect corrugations that are smaller than this region.

The simulations considered in this section aim at illustrating how the electric field surrounding the sample models the aspect of the projected image. They also highlight the unobservability of sample corrugations whose characteristic dimensions are smaller than the resolution Δ_d. We thus justify the lack of direct information on the atomic structure of the sample in the projected images.

To represent the metallic support of the nanotip, we considered a Fermi energy value of 19.1 eV and a work function of 4.5 eV (values for tungsten). The conducting grid is separated from this support by $D = 3.5$ nm and the extraction bias is 25 V. The electron source is represented by a conical tip with 1 nm height. The carbon fiber has a dielectric constant[40] of 16.5 and a work function[40] of 4.82 eV. It is oriented along the x axis and infinite in this direction. Its section in the y-z plane is a square with 1 nm thickness. The potential-energy
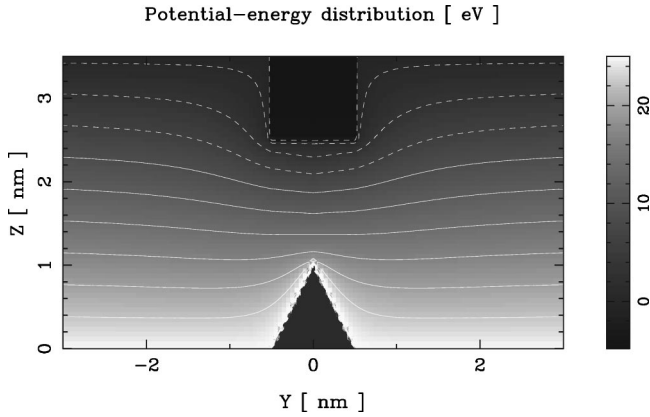
Potential−energy distribution [eV]

FIG. 2. Potential-energy distribution (in eV) in the y-z vertical plane. A 25-V bias is applied over the 3.5 nm separation between the metallic tip holder surface and the sample supporting grid. This grid supports a carbon fiber with 1 nm thickness that is oriented along the x axis.

distribution, computed by overrelaxation,[35] is illustrated in Fig. 2.

In order to highlight the effects of sample polarization on the shape of the projected image, we compared the current density obtained on the 10 cm distant screen when the fiber is not polarized and when polarization is present. The first situation is obtained by characterizing the fiber with a dielectric constant of 1, while in the second situation (for which the potential-energy distribution in Fig. 2 is relevant) the fiber is characterized by a dielectric constant of 16.5. These two results, computed by considering a cancellation radius R of 3.5 nm and m values ranging from -20 until $+20$, are presented in Fig. 3.

The results in Fig. 3 show that the polarization of the fiber is responsible for its projected image to appear brighter. This "sucking-in" effect is due to the attraction of the traveling electrons by the electric field surrounding the fiber when it is polarized. It is interesting to notice that the side of the fiber, when projected geometrically from the point source (as-

sumed here to be the top of the conical emitter), corresponds to a dark line (situated at $y=\pm 2.5$ cm) in the diffraction pattern. This can be related to a destructive interference between the secondary waves that contribute to the image formation (they originate partly from inside and partly from outside the fiber).

In order to justify the lack of direct information on the atomic structure of the fibers in their projected image, we introduced a sinusoidal perturbation in the internal potential of the previously considered fiber and examined its observability in the projected image as a function of the period of the perturbation.

The fiber considered in these simulations has a dielectric constant of 16.5. The internal potential is changed from -4.82 eV to -4.82 eV $+2*\sin(2\pi x/P)*\sin(2\pi y/P)*\sin(2*\pi z/P)$ eV, where P is the period of the perturbation in each direction. Due to the peculiar form of this perturbation, the average of the potential energy in the fiber keeps the same value of -4.82 eV. We have illustrated in Fig. 4 the current density computed on the 10 cm distant screen when the period P is, respectively, 1 nm, 0.5 nm, and 0.25 nm.

We see that the effects of the sinusoidal perturbation are visible for $P=1$ nm. They hardly appear in the second part of Fig. 4. The third part of this figure is nearly identical to the second part of Fig. 3. The resolution limit due to diffraction can be estimated from $\Delta_d=\frac{1}{2}\sqrt{\lambda d}$. By taking $\lambda=0.24$ nm and $d=2$ nm, we find $\Delta_d=0.35$ nm. This accounts for the fact that a sinusoidal perturbation with a period of 0.5 nm hardly induces visible effects, while a perturbation with a period of 0.25 nm cannot be detected in the projected image. These simulations make clear why the potential-energy corrugations associated with the atomic structure of the fiber do not appear in the projected images.

For the atoms to be detected, the resolution limit Δ_d should be smaller than 0.1 nm. This requires us to reduce either λ or d. However, since the local electric field on the nanotip cannot be significantly larger than 10 V/nm, it is not possible to reduce both λ and d arbitrarily. By minimizing

Current Density (r−component) [10^{-8} A / cm2]

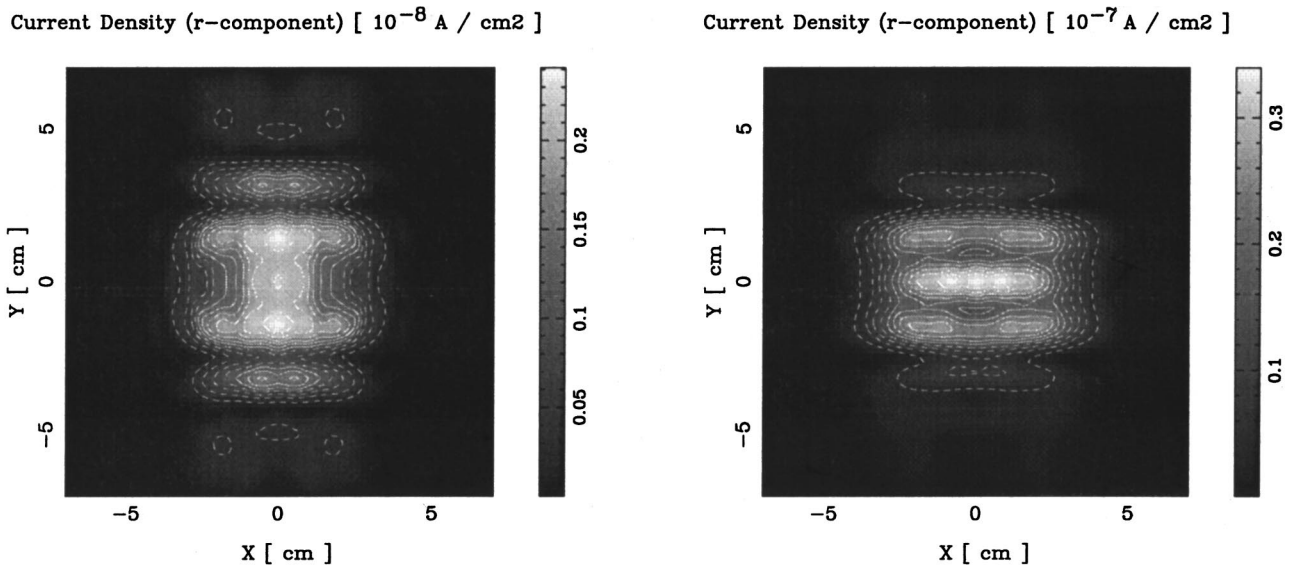Current Density (r−component) [10^{-7} A / cm2]

FIG. 3. Current density (in A/cm^2) on the 10 cm distant screen corresponding to the observation of a carbon fiber with 1 nm thickness under a bias of 25 V. Left part: the fiber is not polarized ($\epsilon=1$). Right part: the fiber is polarized ($\epsilon=16.5$).
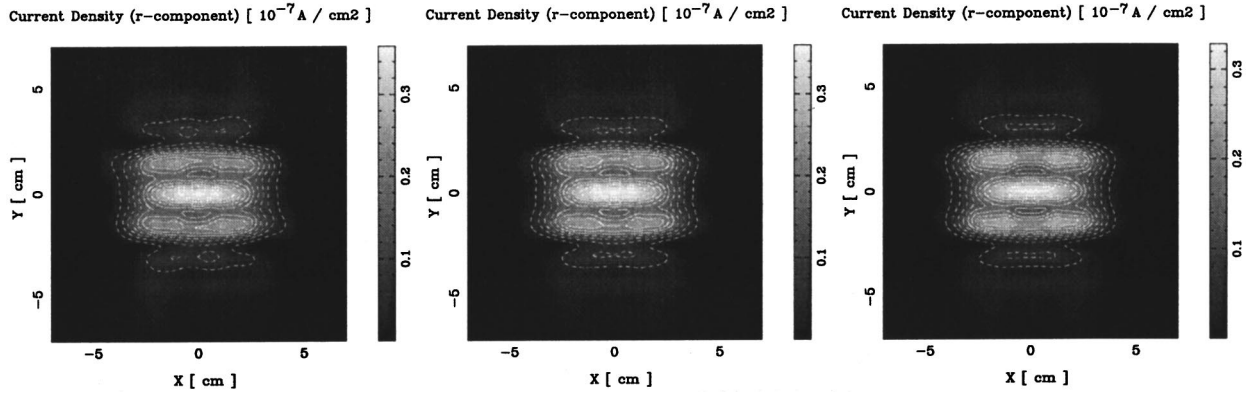
FIG. 4. Current density (in A/cm^2) on the 10 cm distant screen corresponding to the observation of a polarized carbon fiber with 1 nm thickness and modified internal potential under a bias of 25 V. From left to right: the period of the sinusoidal perturbation of the internal potential is, respectively, 1 nm, 0.5 nm, and 0.25 nm.

Δ_d under the condition $(E+W)/d \lesssim 10$ V/nm, a limit of 0.35 nm is found for the resolution of the projection microscope. This limit is not compatible with the direct observation of the atomic structure of a sample by standard projection microscopy.

IV. CONCLUSION

An efficient technique for the simulation of electronic projection microscopy was presented. This technique, that relies on both the transfer-matrix and Green's-function formalisms, can take advantage of a central n-fold symmetry axis.

The technique enables the computation of current densities at arbitrary distances. The computation effort for the electronic scattering can be minimized by confining the electrons, in the part where the scattering occurs, in a cylinder with a radius R as small as physically admissible. Once the scattering is computed, the result is straightforwardly propagated to the imaging screen by using the Green's-function formalism.

This method differs essentially from the Fresnel-Kirchhoff theory in the fact that the empirical point source and the two-dimensional mask are replaced by an accurate transfer-matrix computation, that takes into account the three-dimensional electric field distribution. Breaking through the limits of two-dimensional models, this improved technique enables us to simulate the interaction of the traveling electrons with the electric field surrounding the sample. It also makes it possible to consider three-dimensional corrugations in the sample.

These extended capabilities were used to illustrate the influence of the electric field surrounding a carbon fiber on its projected image (sucking-in effect). The simulations also investigated the observability of corrugations inside the fiber and revealed a critical size for a detection to be possible. These results justify the lack of direct information on the atomic structure in the images obtained by projection microscopy.

ACKNOWLEDGMENTS

APPENDIX: HUYGENS PRINCIPLE IN THE GREEN FORMALISM

Let us consider the stationary Schrödinger equation with the relation defining the associated Green function:

$$\nabla^2_{\mathbf{r}'}\Psi(\mathbf{r}') + \frac{2m}{\hbar^2}[E - V(\mathbf{r}')]\Psi(\mathbf{r}') = 0, \qquad \text{(A1)}$$

$$\nabla^2_{\mathbf{r}'}G(\mathbf{r}',\mathbf{r},E) + \frac{2m}{\hbar^2}[E - V(\mathbf{r}')]G(\mathbf{r}',\mathbf{r},E) = \frac{2m}{\hbar^2}\delta(\mathbf{r}'-\mathbf{r}). \tag{A2}$$

Let us multiply the first equation by $G(\mathbf{r}',\mathbf{r},E)$, the second by $\Psi(\mathbf{r}')$, and subtract the two expressions. When the result is integrated over a volume V that contains $\mathbf{r}$, one finds

$$\int\int\int_V [G(\mathbf{r}',\mathbf{r},E)\nabla^2_{\mathbf{r}'}\Psi(\mathbf{r}')$$
$$-\Psi(\mathbf{r}')\nabla^2_{\mathbf{r}'}G(\mathbf{r}',\mathbf{r},E)]dV' = -\frac{2m}{\hbar^2}\Psi(\mathbf{r}). \tag{A3}$$

By using the Green's formula, this last result becomes

$$\int\int_S \mathbf{n}\cdot[G(\mathbf{r}',\mathbf{r},E)\boldsymbol{\nabla}_{\mathbf{r}'}\Psi(\mathbf{r}')$$
$$-\Psi(\mathbf{r}')\boldsymbol{\nabla}_{\mathbf{r}'}G(\mathbf{r}',\mathbf{r},E)]dS' = -\frac{2m}{\hbar^2}\Psi(\mathbf{r}), \tag{A4}$$

where S is the limiting surface of the volume V and $\mathbf{n}$ is a unit vector normal to S and oriented outwards.

This equation makes it possible to compute the wave function [solution of Eq. (A1)] at a given point $\mathbf{r}$ by using its expression on a surrounding surface S.

*Author to whom correspondence should be addressed. Electronic address: alexandre.mayer@fundp.ac.be

[1] R.H. Fowler and L. Nordheim, Proc. R. Soc. London, Ser. A **119**, 173 (1928).

[2] R.H. Good and E. Müller, *Handbuch der Physik* (Springer-Verlag, Berlin, 1956), Vol. 21, p. 176.

[3] R.E. Burgess, H. Kroemer, and J.M. Houston, Phys. Rev. **90**, 515 (1953).

[4] D.R. Young, Phys. Rev. **113**, 110 (1959).

[5] R. Stratton, Phys. Rev. **135**, A794 (1964).

[6] L.W. Swanson and L.C. Crouser, Phys. Rev. **163**, 622 (1967).

[7] J. He, P.H. Cutler, N.M. Miskovsky, T.E. Feuchtwang, T.E. Sullivan, and M. Chung, Surf. Sci. **246**, 348 (1991).

[8] P.H. Cutler, J. He, N.M. Miskovsky, T.E. Sullivan, and B. Weiss, J. Vac. Sci. Technol. B **11**, 387 (1992).

[9] K.L. Jensen and E.G. Zaidman, J. Vac. Sci. Technol. B **12**, 776 (1993).

[10] A.J. Melmed, Appl. Phys. Lett. **12**, 100 (1968).

[11] V.T. Binh, V. Semet, and N. Garcia, Ultramicroscopy **58**, 307 (1995).

[12] V.T. Binh, S.T. Purcell, N. Garcia, and J. Doglioni, Phys. Rev. Lett. **69**, 2527 (1992).

[13] S.T. Purcell, V.T. Binh, N. Garcia, M.E. Lin, R.P. Andres, and R. Reifenberger, Phys. Rev. B **49**, 17 259 (1994).

[14] N. Garcia, V.T. Binh, and S.T. Purcell, Surf. Sci. Lett. **293**, 884 (1993).

[15] V.T. Binh, N. Garcia, S.T. Purcell, and V. Semet, *Nanosources and Manipulation of Atoms Under High Fields and Temperatures: Applications* (Kluwer, New York, 1993).

[16] V.T. Binh and N. Garcia, Surf. Sci. **320**, 69 (1994).

[17] N. Garcia and H. Rohrer, J. Phys.: Condens. Matter **1**, 3737 (1989).

[18] V.T. Binh, V. Semet, N. Garcia, and L. Bitar, *Optics at the Nanometer Scale*, edited by M. Nieto-Vesperinas and N. Garcia (Kluwer, Dordrecht, 1996), pp. 277–296.

[19] V.T. Binh and V. Semet, Ultramicroscopy **73**, 107 (1998).

[20] A.A. Lucas, H. Morawitz, G.R. Henry, J.P. Vigneron, P. Lambin, P.H. Cutler, and T.E. Feuchtwang, Phys. Rev. B **37**, 10 708 (1988).

[21] A.A. Lucas, H. Morawitz, G.R. Henry, J.P. Vigneron, P. Lambin, P.H. Cutler, and T.E. Feuchtwang, J. Vac. Sci. Technol. A **6**, 296 (1988).

[22] O.J.F. Martin, C. Girard, and A. Dereux, Phys. Rev. Lett. **74**, 526 (1995).

[23] G. Doyen, E. Koetter, J.-P. Vigneron, and M. Scheffler, Appl. Phys. A: Solids Surf. **51**, 281 (1990).

[24] J.P. Vigneron, M. Scheffler, T. Laloyaux, I. Derycke, and A.A. Lucas, Vacuum **41**, 745 (1990).

[25] J.P. Vigneron, F. Forati, D. Andre, A. Castiaux, I. Derycke, and A. Dereux, Ultramicroscopy **61**, 21 (1995).

[26] F. Forati, A. Dereux, J.P. Vigneron, C. Girard, and F. Scheurer, Ultramicroscopy **61**, 57 (1995).

[27] A. Mayer and J.P. Vigneron, Phys. Rev. E **59**, 4659 (1999).

[28] J.P. Vigneron, I. Derycke, T. Laloyaux, P. Lambin, and A.A. Lucas, Scanning Microsc. Suppl. **7**, 261 (1993).

[29] W.D. Sheng and J.B. Xia, J. Phys.: Condens. Matter **8**, 3635 (1996).

[30] J.B. Pendry, *Low Energy Electron Diffraction* (Academic, London, 1974).

[31] T. Laloyaux, A.A. Lucas, J.P. Vigneron, P. Lambin, and H. Morawitz, J. Microsc. **152**, 53 (1988).

[32] P.St.J. Russel, T.A. Birks, and F.D. Lloyds-Lucas, in *Confined Electrons and Photons*, edited by E. Burstein and C. Weisbuch (Plenum, New York, 1995).

[33] A.J. Ward and J.B. Pendry, J. Mod. Opt. **44**, 1703 (1997).

[34] T. Laloyaux, I. Derycke, J.P. Vigneron, P. Lambin, and A.A. Lucas, Phys. Rev. B **47**, 7508 (1993).

[35] A. Mayer and J.P. Vigneron, Phys. Rev. B **56**, 12 599 (1997).

[36] A. Mayer and J.P. Vigneron, J. Phys.: Condens. Matter **10**, 869 (1998).

[37] J. D. Jackson, *Classical Electrodynamics*, 2nd ed. (John Wiley & Sons, New York, 1962), p. 427.

[38] G.N. Watson, *Theory of Bessel Functions*, 2nd ed. (Cambridge University Press, Cambridge, England, 1966).

[39] A. Mayer and J.-P. Vigneron, J. Vac. Sci. Technol. B **17**, 506 (1999).

[40] W.E. Forsythe, *Smithsonian Physical Tables*, 9th ed. (Smithsonian Institution, Washington, D.C., 1954), pp. 427 and 635.